Drug Self-Association Modulates the Cellular Bioavailability of DNA Minor Groove-Directed Terbenzimidazoles

Qasim A. Khan,[†] Christopher M. Barbieri,[†] Annankoil R. Srinivasan,[†] Yuh-Hwa Wang,[‡] Edmond J. LaVoie,[§,||] and Daniel S. Pilch*[,†,||]

Departments of Pharmacology and Biochemistry, University of Medicine and Dentistry of New Jersey, Robert Wood Johnson Medical School, 675 Hoes Lane, Piscataway, New Jersey 08854-5635, Department of Pharmaceutical Chemistry, Rutgers-The State University of New Jersey, Piscataway, New Jersey 08855, and Cancer Institute of New Jersey, New Brunswick, New Jersey 08901

Received May 2, 2006

The terbenzimidazoles are a class of anticancer agents that bind in the DNA minor groove. These compounds also exhibit a propensity for self-association, which can potentially impact their cellular bioavailabilities and activities. We have explored this possibility by using a broad range of biophysical and cytological techniques to characterize the self-association and cellular uptake properties of two terbenzimidazole analogues, 5-phenylterbenzimidazole (5PTB) and 5-phenyl-2′-(indolo-6-yl)bibenzimidazole (5P2′IBB). Concentration- and temperature-dependent fluorescence spectroscopy, dynamic light scattering, and transmission electron microscopy studies reveal that 5PTB and 5P2′IBB exhibit differing self-association properties. In this connection, 5PTB exhibits an enhanced propensity for self-association and forms larger and more stable aggregates than 5P2′IBB. In addition, the net uptake of 5PTB into human lymphoblast cells is diminished relative to that of 5P2′IBB. These observations suggest that the self-association properties of terbenzimidazoles modulate the cellular bioavailabilities of the compounds, with enhanced self-association propensity and aggregate size leading to reduced cellular bioavailability.

Introduction

Many classes of cytotoxic agents that have the potential to become effective anticancer drugs are hydrophobic, a property that is typically associated with poor solubility in aqueous medium. The limited water solubility of hydrophobic compounds results from their propensities to form aggregates in solution via a myriad of self-association reactions.[1−8] Furthermore, the propensity for aggregation tends to increase with increasing ionic strength.[2] The success of any anticancer drug requires that it reaches its molecular target at concentrations sufficient to induce a potent therapeutic response. A key factor toward achieving this goal is tumor and cellular bioavailability, a factor that is likely to be impacted by drug self-association properties. It is, therefore, important to understand drug aggregation behavior in solution and how this behavior correlates with cellular bioavailability.

The terbenzimidazoles are a class of anticancer agents that bind in the minor groove of duplex DNA.[9−11] In the present study, we characterize and contrast the self-association and cellular uptake properties of two terbenzimidazole analogues (5-phenylterbenzimidazole (5PTB) and 5-phenyl-2′-(indolo-6-yl)bibenzimidazole (5P2′IBB)), whose chemical structures differ only with respect to the identity of the atom at the 3″-position, with this atom being nitrogen in 5PTB and carbon in 5P2′IBB (Figure 1). Our results indicate that 5PTB has a greater propensity for self-association and forms larger and more stable aggregates than 5P2′IBB. In addition, the net uptake of 5PTB into RPMI 8402 human lymphoblast cells is diminished relative to that of 5P2′IBB, an observation that we attribute to the comparatively enhanced aggregation properties of 5PTB. Viewed as a whole, our data highlight drug self-association as a potentially key determinant of cellular bioavailability and, therefore, drug activity.

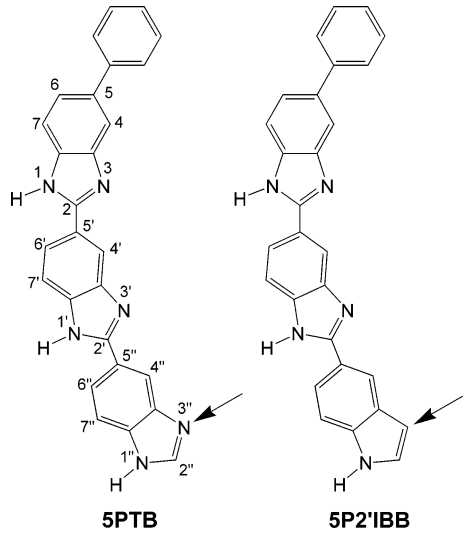

Figure 1. Chemical structures of 5PTB and 5P2′IBB, with the atomic numbering indicated in the 5PTB structure (left). An arrow points to the 3″-position of each compound and highlights the sole difference between the structures of the two compounds.

Materials and Methods

5PTB and 5P2′IBB. 5PTB and 5P2′IBB were synthesized and purified as described previously.[12,13] Stock solutions of these compounds were prepared in dimethyl sulfoxide (DMSO) and stored at −20 °C.

Steady-State Fluorescence Spectroscopy. All steady-state fluorescence measurements were conducted on an AVIV model ATF105 spectrofluorometer (AVIV Biomedical, Lakewood, NJ) equipped with a thermoelectrically controlled cell holder. A quartz cell with a 1 cm path length in both the excitation and

* To whom correspondence should be addressed. Tel: 732-235-3352. Fax. 732-235-4073. E-mail: pilchds@umdnj.edu.
[†] Department of Pharmacology, Robert Wood Johnson Medical School.
[‡] Department of Biochemistry, Robert Wood Johnson Medical School.
[§] Rutgers University.
[||] Cancer Institute of New Jersey.

10.1021/jm060520q CCC: $33.50
Published on Web 07/14/2006

emission directions was used for all measurements unless noted otherwise. In all of the fluorescence experiments, experimental solutions of the compound were preheated at 95 °C for 5 min and slowly cooled to the desired experimental temperature over a period of 2−4 h. Temperature- and concentration-dependent fluorescence experiments were conducted in EKME buffer containing 10 mM EPPS (pH 7.5), 100 mM KCl, 5 mM $MgCl_2$, and 0.1 mM EDTA. For 5PTB, the excitation and emission wavelengths were 340 and 407 nm, respectively. For 5P2′IBB, the excitation and emission wavelengths were 360 and 420 nm, respectively. The excitation and emission slit widths were 2 and 5 nm, respectively. Temperature-dependent measurements were conducted by raising the temperature of solutions containing 1.0 μM ligand in 2.0 °C increments, with the solutions being allowed to equilibrate for 10 min at each temperature setting. Following equilibration, the average fluorescence emission intensity was recorded over a period of 30 s. Concentration-dependent fluorescence studies were conducted at temperatures of 20, 30, and 40 °C using compound concentrations that ranged from 0.3 to 3.0 μM. At each temperature and compound concentration, the average emission intensity was recorded over a period of 60 s. All measured fluorescence emission intensities were corrected by subtraction of the intensity corresponding to the buffer alone.

Transmission Electron Microscopy (TEM). At room temperature, 5 μL aliquots of EKME solutions containing 5PTB or 5P2′IBB at concentrations ranging from 5 to 100 μM were applied to copper mesh grids (Electron Microscopy Sciences, Fort Washington, PA) covered with a thin carbon film as previously described.[14] The samples were then negatively stained with 2% uranyl acetate for 1 min and blotted dry. Micrographs were acquired on a JEOL 1200 EX transmission microscope at 80 kV.

Dynamic Light Scattering (DLS). DLS measurements were conducted in EKME buffer at 25 °C on a DynaPro-MS800 dynamic light scattering instrument (Protein Solutions, Lakewood, NJ), with an argon laser wavelength of 830 nm and a detector angle of 90°. Typical sample volumes were 20 μL and compound concentrations ranged from 0.5 to 5.0 μM. Each measurement consisted of at least 20 independent readings, with each reading being 10 s in duration. All measurements were conducted in quintuplicate. The data were analyzed using the DynaPro Instrument Control Software for Molecular Research (DYNAMICS version 5.26.60). Prior to their use in DLS experiments, all ligand solutions were preheated at 95 °C for 5 min and slowly cooled to 25 °C over a period of 4 h.

Cellular Uptake and Efflux Studies. In the uptake studies, human lymphoblast RPMI 8402 cells (exponentially growing at $\sim 10^6$ cells/mL in RPMI 1640 medium supplemented with 10% fetal bovine serum) were treated with 1.0 μM 5PTB or 5P2′IBB for 0.5, 1, 2, or 4 h. Following treatment, the cells were pelleted, and the pellets were washed twice with phosphate-buffered saline (pH 7.4). Lysis buffer (Promega, Madison, WI) was then added, and the cells were lysed by repeated freeze−thaw cycles, followed by incubation on ice for 15 min. The cell lysates were centrifuged at 15 000 rpm for 20 min at 4 °C. The supernatants were collected and diluted 30-fold into ENE buffer containing 10 mM EPPS (pH 7.5), 100 mM NaCl, and 0.1 mM EDTA. The fluorescence intensities of the resulting samples were measured at 25 °C. In these measurements, the excitation and emission wavelengths were 340 and 405 nm, respectively. The slit widths were 5 nm in both the excitation and emission directions, and the cell path length was 1.0 cm in the excitation direction and 0.2 cm in the emission direction. All measured fluorescence intensities were corrected by subtractiing the intensity corresponding to the buffer alone. Standard curves of fluorescence intensity versus compound concentration were generated by making 30-fold dilutions of mock-treated cell lysates in ENE buffer and adding known concentrations of the compound. The standard curves were fit by linear regression, with the resulting equations being used to calculate intracellular concentrations of compound from the measured fluorescence intensities of the treated cell lysates. The total number of cells following treatment for each time period was assayed using a BCA protein assay kit (Pierce, Rockford, IL). In all cases, the number of cells was similar (to within an uncertainty of ±10%).

In the efflux studies, exponentially growing RPMI 8402 cells were treated as described above. Following treatment, the cells were washed twice with phosphate-buffered saline (pH 7.4) and replenished with fresh medium. Over a time period of 0 to 4 h, 600 μL aliquots of the medium were removed, and their fluorescence intensities were recorded using the same acquisition parameters described above.

Fluorescence Microscopy. Exponentially growing RPMI 8402 cells (at approximately 10^6 cells/mL) were treated with 1.0 μM 5PTB or 5P2′IBB for 2 h. The cells were then examined by fluorescence microscopy using an Olympus model IX70 microscope equipped with a standard DAPI filter set (Chroma Technology Corp., Rockingham, VT). An Olympus CPLAN 40X/0.6 RC3 objective was used to obtain relief contrast images of the RPMI 8402 cells as well as to visualize the incorporation of the two compounds into the chromosomal DNA within the nucleus.

Results and Discussion

Both 5PTB and 5P2′IBB self-associate, with the aggregates formed by 5PTB being thermally more stable than those formed by 5P2′IBB. We monitored the temperature dependence of the fluorescence emission intensities of 5PTB and 5P2′IBB at a concentration of 1.0 μM. The resulting fluorescence melting profiles are shown in Figure 2A. Note that the fluorescence intensity of each compound increases cooperatively with increasing temperature, an observation consistent with the self-association of each compound in a manner that is driven, at least in part, by stacking interactions between the aromatic (i.e., benzimidazole and indole) functionalities. In addition, the melting profiles of both compounds are biphasic. We assign the first phase to the dissociation of higher order aggregates into lower order aggregates and the second phase to the dissociation of the lower order aggregates into monomers. Thus, the self-association of both compounds goes beyond the level of simple dimerization. The first derivatives of the melting profiles are shown in the inset to Figure 2A. The temperatures corresponding to the maxima of such first-derivative profiles (T_{max}) provide estimates for the midpoint temperatures of the melting transitions. An inspection of the inset in Figure 2A reveals T_{max} values of 45 and 71 °C for the two melting transitions of 5P2′IBB, with the corresponding T_{max} values being 57 and 87 °C for the two melting transitions of 5PTB. Thus, the aggregates formed by 5PTB are thermally more stable than those formed by 5P2′IBB.

5PTB self-associates with a greater affinity than 5P2′IBB. The results described in the preceding section suggest that at a given temperature 5P2′IBB has a reduced propensity for self-association relative to 5PTB. We further explored this possibility by monitoring the observed molar emissivity ($[I]_{obs}$) of each compound at 30 °C as a function of compound concentration. For meaningful comparisons, we normalized the $[I]_{obs}$ values

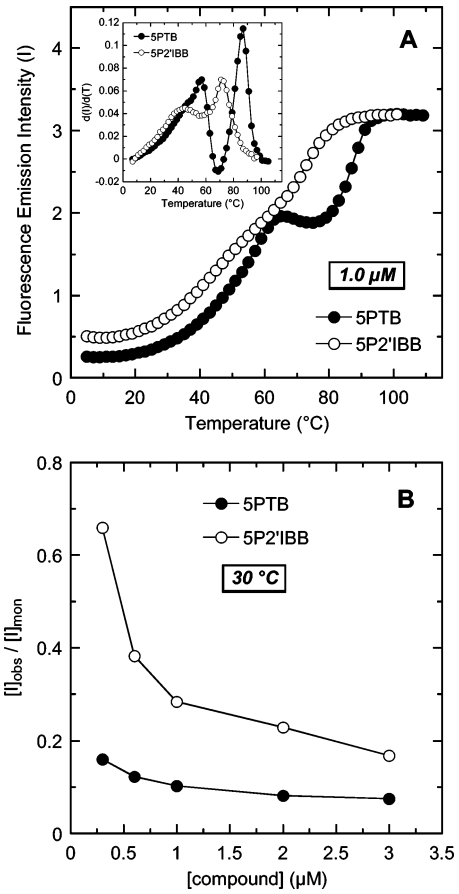

Figure 2. (A) Fluorescence melting profiles of 5PTB (●) and 5P2′IBB (○) at a concentration of 1.0 μM. The inset shows the first derivatives of the melting profiles. (B) Concentration dependence of the molar emissivities ([*I*]) of 5PTB (●) and 5P2′IBB (○) at 30 °C. $[I]_{obs}$ denotes the observed molar emissivity, whereas $[I]_{mon}$ denotes the molar emissivity of the monomeric form of each compound. In all of the depicted experiments, the solution conditions were 10 mM EPPS (pH 7.5), 100 mM KCl, 5 mM $MgCl_2$, and 0.1 mM EDTA.

obtained for each compound relative to the corresponding [*I*] value for the monomeric form of the compound ($[I]_{mon}$). The value of $[I]_{mon}$ at 30 °C for each compound was derived from the high-temperature baselines of melting profiles conducted over a range of compound concentrations (not shown). Such baselines provide a measure of how the fluorescence emission intensities of the monomeric forms of the compounds vary with temperature. Figure 2B shows the dependence of $[I]_{obs}/[I]_{mon}$ on compound concentration at 30 °C. Note that increasing compound concentration results in a corresponding decrease in $[I]_{obs}/[I]_{mon}$, an observation reflecting a concentration-induced increase in the fraction of total compound that exists in the self-associated rather than the monomeric state. Furthermore, at each of the compound concentrations examined, the value of $[I]_{obs}/[I]_{mon}$ for 5PTB is lower than the corresponding value for 5P2′IBB. In other words, at each of the compound concentrations examined, the fraction of total 5PTB that exists in the self-associated state is greater than the corresponding fraction of total 5P2′IBB.

The result described above implies that 5PTB self-associates with a greater affinity than 5P2′IBB. The self-association constants (K_{Self}) for 5PTB and 5P2′IBB can be derived by recasting data such as those shown in Figure 2B as linear plots of $\sqrt{\frac{[I]_{mon}-[I]_{obs}}{[compound]}}$ versus $[I]_{mon} - [I]_{obs}$, and analyzing these plots with the following formalism based on a model for self-association of the compounds to form *n*-mers:[4,15]

$$\sqrt{\frac{[I]_{mon} - [I]_{obs}}{[compound]}} = \sqrt{\frac{K_{self}}{2([I]_{mon} - [I]_{dim})}} \times \{2([I]_{mon} - [I]_{dim}) + [I]_{mon} - [I]_{obs}\} \quad (1)$$

In this relationship, $[I]_{dim}$ denotes the molar emissivity of the dimeric form of the compound. Note that the formalism described by eq 1 is predicated on the reasonable assumption that each compound molecule binds to the growing aggregate with an identical affinity constant of K_{Self}. Values of K_{Self} can be derived from the slopes (*s*) and *x*-intercepts (*x*) of $\sqrt{\frac{[I]_{mon}-[I]_{obs}}{[compound]}}$ versus $[I]_{mon} - [I]_{obs}$ plots using the following relationship.

$$K_{Self} = xs^2 \quad (2)$$

Figure 3 show plots of $\sqrt{\frac{[I]_{mon}-[I]_{obs}}{[compound]}}$ versus $[I]_{mon} - [I]_{obs}$ for 5PTB (A) and 5P2′IBB (B) at 20, 30, and 40 °C. The values of K_{Self} derived from linear regression analyses of these plots and subsequent application of eq 2 are listed in Table 1. At each temperature examined, the value of K_{Self} for 5PTB is at least 24-fold greater than that for 5P2′IBB, an observation confirming that 5PTB self-associates with a greater affinity than 5P2′IBB.

Self-association of 5PTB and 5P2′IBB is enthalpy driven, with the enhanced self-association affinity of 5PTB relative to that of 5P2′IBB also being enthalpic in origin. An additional feature that emerges from the data listed in Table 1 is that the self-association affinity (K_{Self}) of each compound diminishes with increasing temperature. Specifically, a temperature increase from 20 to 40 °C results in a 19-fold decrease in the self-association affinity of 5PTB and a 14-fold decrease in the self-association affinity of 5P2′IBB. This temperature-induced reduction in the self-association affinities of the two compounds implies that the self-association reactions are accompanied by an exothermic (favorable) change in enthalpy. We explored this implication further by characterizing the thermodynamics of the self-association reactions of both compounds. To this end, we analyzed the temperature dependence of K_{Self} using the following van't Hoff relationship

$$\ln(K_{self}) = \left(-\frac{\Delta H}{R}\right)\frac{1}{T} + \frac{\Delta S}{R} \quad (3)$$

In this relationship, ΔH and ΔS denote the self-association enthalpy and entropy changes, respectively, with *R* being the gas constant. Equation 3 postulates that plots of $\ln(K_{Self})$ versus $1/T$ (also termed van't Hoff plots) will be linear, with the slopes and *y*-intercepts of these plots yielding estimates for ΔH and ΔS, respectively. Figure 3C shows the van't Hoff plots for 5PTB and 5P2′IBB constructed using the temperature-dependent K_{Self} data listed in Table 1. The values of ΔH and ΔS derived from linear regression analyses of these plots and subsequent application of eq 3 are listed in Table 2. In addition, Table 2 also lists the free energy changes that accompany the self-association reactions at 30 °C (ΔG_{30}). These ΔG_{30} values were derived using the corresponding values of K_{Self} and the following standard relationship

$$\Delta G = -RT \ln(K_{Self}) \quad (4)$$

An inspection of the thermodynamic data in Table 2 reveals favorable (negative or exothermic) ΔH values for the self-

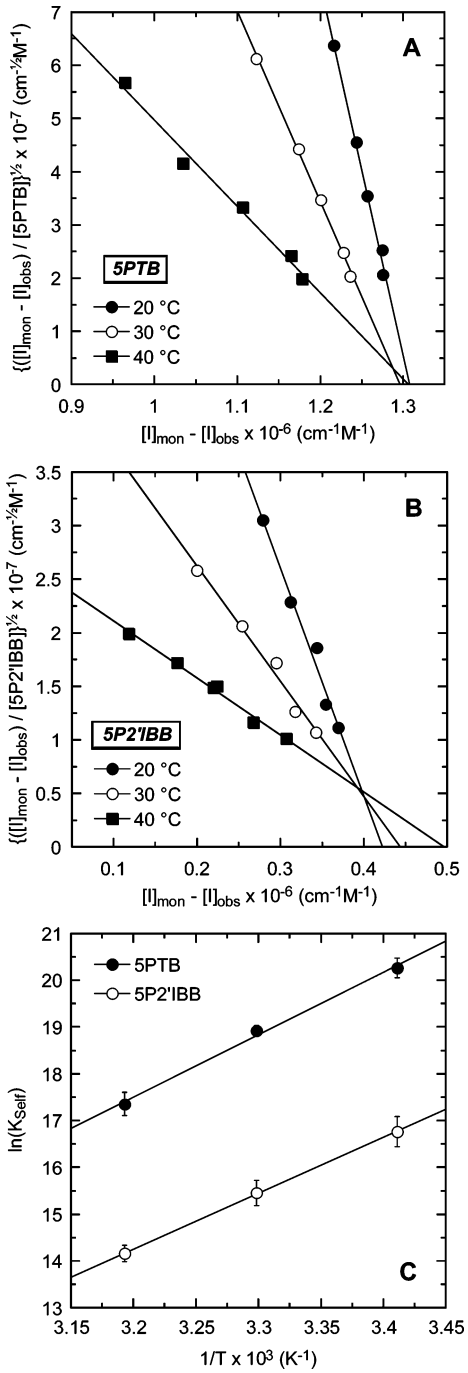

Figure 3. Analysis of the concentration dependence of the 5PTB (A) and 5P2′IBB (B) fluorescence at 20 (●), 30 (○), and 40 °C (■) for the purposes of determining self-association constants (K_{Self}) using eqs 2 and 3. The solid lines in (A) and (B) reflect the fits of the data with eq 1. (C) van't Hoff plots depicting the temperature dependence of K_{Self} for the self-association of 5PTB (●) and 5P2′IBB (○). The solid lines reflect the fits of the data with eq 3. In all of the depicted experiments, the solutions conditions were as described in the legend to Figure 2.

association of both compounds. In contrast, the corresponding ΔS values are unfavorable (negative). However, these unfavorable entropic penalties are more than offset by the favorable enthalpic contributions to self-association, with the net result being favorable (negative or exergonic) ΔG_{30} values. Taken together, these results indicate that the self-association reactions of both 5PTB and 5P2′IBB are enthalpy driven. Recall that our fluorescence melting studies were consistent with stacking interactions between aromatic functionalities playing a role in stabilizing the aggregates formed by each of the two compounds.

Table 1. Temperature Dependence of the Self-Association Constants (K_{Self}) of 5PTB and 5P2′IBB[a]

compd	temp (°C)	K_{Self} (M^{-1})
5PTB	20	$(6.3 \pm 1.5) \times 10^8$
5PTB	30	$(1.6 \pm 0.2) \times 10^8$
5PTB	40	$(3.4 \pm 1.0) \times 10^7$
5P2′IBB	20	$(1.9 \pm 0.7) \times 10^7$
5P2′IBB	30	$(5.1 \pm 1.6) \times 10^6$
5P2′IBB	40	$(1.4 \pm 0.3) \times 10^6$

[a] The values of K_{Self} were derived from the slopes (s) and x-intercepts (x) of the linear plots shown in panels A and B of Figure 3 using eq 2. The indicated uncertainties in K_{Self} reflect the maximum possible errors in x and s as propagated through this equation.

Table 2. Thermodynamic Profiles for the Self-Association of 5PTB and 5P2′IBB at 30 °C

compd	ΔH (kcal/mol)[a]	ΔS (kcal/mol·K)[a]	ΔG_{30} (kcal/mol)[b]
5PTB	-26.5 ± 1.4	-0.0498 ± 0.0055	-11.4 ± 0.1
5P2′IBB	-23.7 ± 0.4	-0.0476 ± 0.0012	-9.3 ± 0.2

[a] The values of ΔH and ΔS were derived from the slopes (s) and y-intercepts (y) of the van't Hoff plots shown in Figure 3C using eq 3. The indicated uncertainties in ΔH and ΔS reflect the maximum possible errors in s and y as propagated through this equation. [b] The values of ΔG at 30 °C (ΔG_{30}) were derived using the appropriate values of K_{Self} from Table 1 and eq 4. The indicated uncertainties in ΔG_{30} reflect the maximum possible errors in K_{Self} as propagated through this equation.

Such a role is also consistent with the enthalpic nature of the thermodynamic driving force for the self-association reactions because stacking interactions between aromatic functionalities are typically manifested enthalpically.

The ΔG_{30} values listed in Table 2 indicate that the aggregates formed by 5PTB at 30 °C are 2.1 kcal/mol more stable than those formed by 5P2′IBB. Note that the unfavorable entropic contributions to self-association are similar in magnitude for the two compounds, with the difference between them being within experimental uncertainty. In contrast, the favorable enthalpic contribution to the self-association of 5PTB is 2.8 kcal/mol greater in magnitude than the corresponding contribution to the self-association of 5P2′IBB. Thus, the 2.1 kcal/mol enhanced stability of the aggregates formed by 5PTB relative to those formed by 5P2′IBB is enthalpic in origin. This observation may reflect enhanced stacking interactions in the 5PTB relative to the 5P2′IBB aggregates and/or the presence of other enthalpically manifested interactions (e.g., hydrogen bonding interactions) in the 5PTB but not the 5P2′IBB aggregates.

DLS measurements suggest that the aggregates formed by 5PTB are approximately twice the size of those formed by 5P2′IBB. The principles behind the DLS technique are based on the Stokes−Einstein relation between the friction coefficient (f) and the translational diffusion coefficient (D_t) of a molecule. DLS provides a direct measure of D_t in a manner that is dependent on molecular size but independent of molecular shape. The dependence of D_t on molecular size is an inverse proportionality, with larger molecules diffusing more slowly than smaller ones. These properties make DLS a useful tool for the detection and characterization of molecular aggregates. We conducted DLS studies on solutions containing either 5PTB or 5P2′IBB at concentrations ranging from 0.5 to 5 μM. These measurements yielded D_t values of $(1.13 \pm 0.11) \times 10^{-8}$ and $(2.40 \pm 0.16) \times 10^{-8}$ cm^2/s for 5PTB and 5P2′IBB, respectively. This roughly 2-fold differential between the D_t values of 5PTB and 5P2′IBB is consistent with the aggregates formed by 5PTB being approximately twice the size of the aggregates formed by 5P2′IBB.

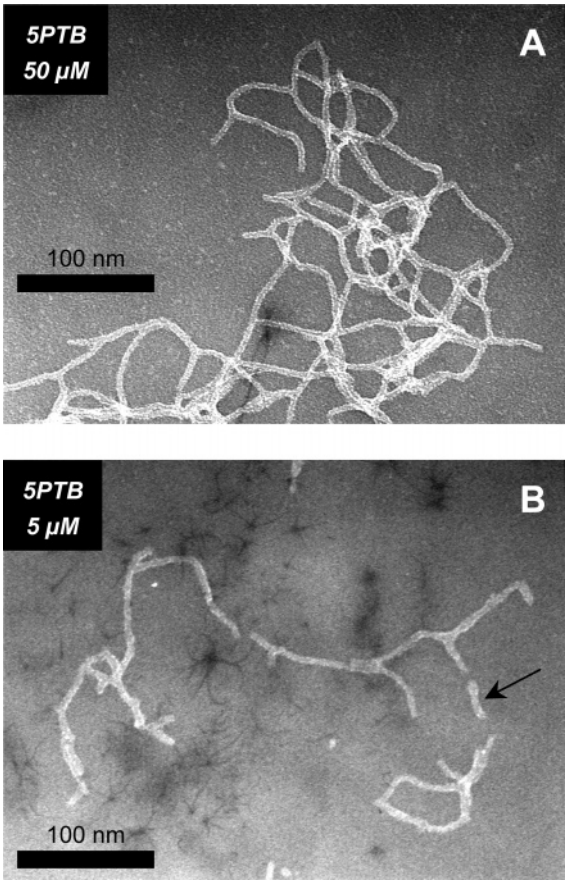

Figure 4. Transmission electron micrographs of the aggregates formed by 5PTB at concentrations of either 50 (A) or 5 (B) μM. The black bar corresponds to 100 nm. The arrow in (B) points to an aggregate fragment approximately 330 Å in length.

Structural characterization of the aggregates formed by 5PTB using TEM. We used TEM to characterize the structural nature of the aggregates formed by 5PTB. Figure 4 shows the resulting electron micrographs obtained at two different 5PTB concentrations (5 and 50 μM). Note that 5PTB forms a network of filaments, with the number and length of the filaments forming the network being greater at 50 μM (Figure 4A) than at 5 μM (Figure 4B). In addition, all of the individual filaments have a fairly uniform width of approximately 55−60 Å, a width that is approximately three times the longest dimension of a single 5PTB molecule, which is approximately 20 Å. It should be emphasized that the 5PTB images depicted in Figure 4 do not reflect aggregates that have precipitated out of solution. We also conducted TEM studies of 5P2′IBB over a range of concentrations from 5 to 100 μM. However, these studies did not produce any detectable images of nonprecipitated aggregates. This inability to produce detectable images of nonprecipitated 5P2′IBB aggregates may reflect poor adherence to the carbon-coated grids on the part of these aggregates.

It is possible that the filamentous structures observed in the TEM images correspond to linear arrays of 5PTB molecules that are stabilized by a combination of stacking and hydrogen-bonding interactions between aromatic functionalities. Although the lengths of the filamentous structures appear to be heterogeneous and are difficult to ascertain, one particular 5PTB filament in Figure 4B (identified by the arrow) is an isolated fragment approximately 330 Å in length. On the basis of the molecular interpretation for the filamentous structures noted above, this filament fragment would reflect a linear array containing on the order of 300 5PTB molecules because (i) stacking interactions between aromatic functionalities are maximized when the separation between the aromatic groups is 3.4 Å and (ii) the filament width is approximately three times that of the longest dimension of a single 5PTB molecule. Given the significantly shorter length of the 330 Å filament relative to that of the other 5PTB filaments in Figure 4, the average number of 5PTB molecules in the larger filaments is likely on the order of thousands rather than hundreds.

Recall that 5P2′IBB molecules contain C3″ atoms in place of the N3″ atoms that are present in 5PTB molecules (Figure 1). It is likely that this chemical difference results in 5P2′IBB having diminished capabilities to form hydrogen-bonding interactions relative to that of 5PTB. Such reduced hydrogen bonding capabilities may account for the reduced thermal and enthalpic stabilities and roughly 2-fold smaller size of the aggregates formed by 5P2′IBB relative to those formed by 5PTB.

Net uptake of 5P2′IBB into RPMI 8402 human lymphoblast cells exceeds that of 5PTB. We monitored the net uptake of 5PTB and 5P2′IBB into RPMI 8402 cells after treatment with 1 μM compound for periods of 0.5, 1, 2, and 4 h. In this connection, we used the intrinsic fluorescence of the compounds as a vehicle for determining the amount of intracellular compound. The resulting time course for the uptake of the two compounds is shown in Figure 5A. After each treatment time, the uptake of 5PTB is essentially constant at approximately 3% of the total moles of added compound. In contrast, the uptake of 5P2′IBB ranges from approximately 18% after 0.5 h of treatment to approximately 30% after 4 h of treatment. Thus, over the time period examined, the uptake of 5P2′IBB exceeds that of 5PTB by approximately 6- to 10-fold. Recall that 5PTB has a greater propensity for self-association than 5P2′IBB. Furthermore, the aggregates formed by 5PTB are larger in size than those formed by 5P2′IBB. It is likely that these differential self-association properties account for the enhanced uptake of 5P2′IBB relative to that of 5PTB, particularly because the monomeric forms of the two compounds are similar in both size and chemical nature. An important next step will be to explore the generality of our cellular uptake results with regard to other tumor cell lines.

We recognize that the difference in net cellular uptake noted above reflects contributions from potential differences in influx and/or efflux. In an effort to determine the contributions, if any, from differential efflux to our observed difference in net uptake, we monitored the net efflux of 5PTB and 5P2′IBB from RPMI 8402 cells over a time period of up to 4 h. Significantly, these studies (not shown) revealed no difference in the efflux properties of the two compounds. Thus, the difference in net cellular uptake between 5PTB and 5P2′IBB reflects a difference in influx and not efflux.

Chromosomal DNA is the intracellular target of both 5PTB and 5P2′IBB. We used fluorescence microscopy to map the localization of 5PTB and 5P2′IBB inside RPMI 8402 cells. Figure 5 shows representative fluorescence micrographs of RPMI 8402 cells treated for 2 h with either 1 μM 5PTB (B−D) or 1 μM 5P2′IBB (E−G). The nuclear staining exhibited by both compounds is indicative of their localization to the nuclei of the cells. As expected, mock-treated cells were not fluorescent (results not shown). The cells identified by the arrows in Figures 5C and F are in the telophase of mitosis. Note that both 5PTB and 5P2′IBB are specifically staining the chromosomal DNA in these cells. This observation indicates that the nuclear staining exhibited by the compounds is not the result of being simply trapped in the nuclei but rather due to specific interactions with chromosomal DNA. Another significant feature of Figure 5 is

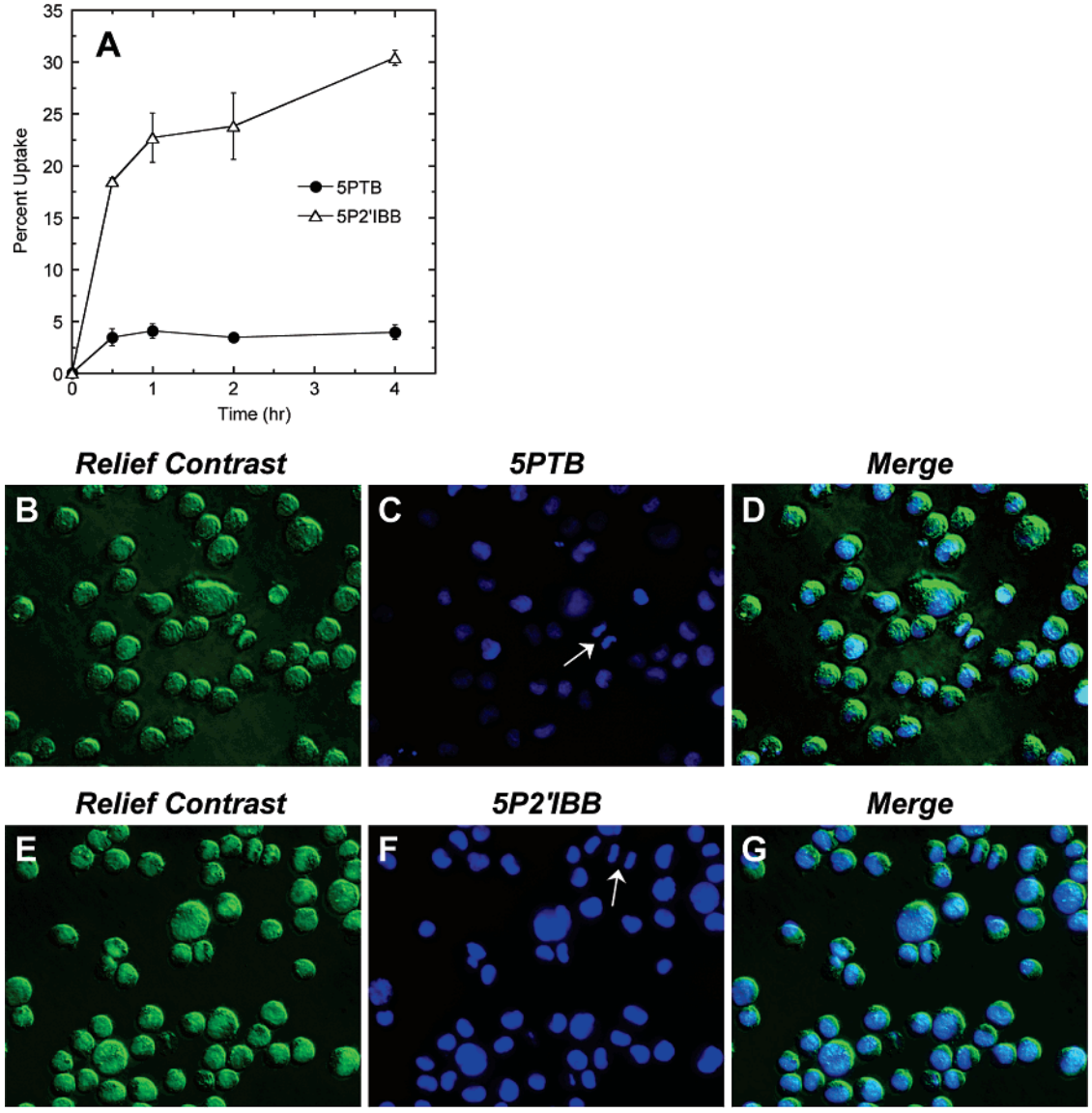

Figure 5. (A) Time course for the net uptake of 5PTB (●) and 5P2′IBB (△) into RPMI 8402 human lymphoblast cells treated for the indicated times with a 1.0 μM concentration of compound. Percent uptake reflects the percentage of the total number of added moles of compound taken up by the cells. (B−G) Fluorescence micrographs of RPMI 8402 cells treated with 1.0 μM 5PTB (B−D) or 5P2′IBB (E−G) for 2 h. (B) and (E) depict relief contrast images of the treated cells, whereas (C) and (F) show images in which compound fluorescence is being detected. (D) and (G) show merged images of the relief contrast and compound signals. The arrows in (C) and (F) point to cells in the telophase of mitosis. Both 5PTB and 5P2′IBB are detected in the nuclei of the cells bound to the chromosomal DNA.

the greater degree of nuclear fluorescence in cells treated with 5P2′IBB (Figure 5F) relative to that of those treated with 5PTB (Figure 5C). This difference in nuclear fluorescence is consistent with our cellular uptake studies described above, which revealed a greater net uptake of 5P2′IBB relative to that of 5PTB.

Concluding Remarks

Previous studies have indicated that the cytotoxic activity of 5P2′IBB exceeds that of 5PTB.[12] However, this differential cytotoxicity could not be explained by a corresponding difference in apparent DNA binding affinity,[12] a binding parameter whose magnitude decreases with increasing propensity for drug self-association.[4] In this study, we show that 5PTB and 5P2′IBB differ with regard to their self-association and cellular uptake properties. 5PTB exhibits a greater propensity for self-association and forms larger and more stable aggregates than 5P2′IBB. Furthermore, the net uptake of 5PTB into cancer cells is diminished relative to that of 5P2′IBB. These collective results suggest that self-association properties modulate the cellular bioavailabilities of the two compounds, with enhanced self-association propensity and aggregate size leading to reduced cellular bioavailability and, ultimately, reduced DNA binding and cytotoxicity. Drug self-association properties can also influence bioavailability in vivo.[8] In this regard, an important next step will be to evaluate the impact of terbenzimidazole self-association properties on the pharmacokinetics and pharmacodynamics of the compounds in vivo.

Acknowledgment. We thank Dr. Loren Runnels for his assistance with the fluorescence microscopy experiments, Dr. Eddy Arnold for granting us access to his DLS instrument, and Yulia Volovik Frenkel for her assistance with the DLS experiments. This work was supported by National Institutes of Health Grants CA097123 (to D.S.P.), CA098127 (to E.J.L.), and CA085826 (to Y.-H.W.) and American Cancer Society Grant RSG-99-153-04-CDD (to D.S.P.).

References

(1) Barthelemy-Clavey, V.; Maurizot, J.-C.; Dimicoli, J.-L.; Sicard, P. Self-Association of Daunorubicin. *FEBS Lett.* **1974**, *46*, 5−10.

(2) Gough, A. N.; Jones, R. L.; Wilson, W. D. Dimerization of Coralyne and Its Propyl Analogue and Their Association with DNA. *J. Med. Chem.* **1979**, *22*, 1551−1554.

(3) Martin, S. R. Absorption and Circular Dichroic Spectral Studies on the Self-Association of Daunorubicin. *Biopolymers* **1980**, *19*, 713−721.

(4) Chaires, J. B.; Dattagupta, N.; Crothers, D. M. Self-Association of Daunomycin. *Biochemistry* **1982**, *21*, 3927−3932.

(5) Loontiens, F. G.; Regenfuss, P.; Zechel, A.; Dumortier, L.; Clegg, R. M. Binding Characteristics of Hoechst 33258 with Calf Thymus DNA, poly[d(A-T)], and d(CCGGAATTCCGG): Multiple Stoichiometries and Determination of Tight Binding with a Wide Spectrum of Site Affinities. *Biochemistry* **1990**, *29*, 9029−9039.

(6) Pilch, D. S.; Martin, M.-T.; Nguyen, C. H.; Sun, J.-S.; Bisagni, E.; Garestier, T.; Hélène, C. Self-Association and DNA-Binding Properties of Two Triple Helix-Specific Ligands: Comparison of a Benzo[*e*]pyridoindole and a Benzo[*g*]pyridoindole. *J. Am. Chem. Soc.* **1993**, *115*, 9942−9951.

(7) Pilch, D. S.; Kirolos, M. A.; Liu, X.; Plum, G. E.; Breslauer, K. J. Berenil [1,3-Bis-(*4*′-amidinophenyl)triazene] Binding to DNA Duplexes and to a RNA Duplex: Evidence for Both Intercalative and Minor Groove Binding Properties. *Biochemistry* **1995**, *34*, 9962−9976.

(8) Volovik Frenkel, Y.; Clark, A. D.; Das, K.; Wang, Y.-H.; Lewi, P. J.; Janssen, P. A. J.; Arnold, E. Concentration and pH Dependent Aggregation of Hydrophobic Drug Molecules and Relevance to Oral Bioavailability. *J. Med. Chem.* **2005**, *48*, 1974−1983.

(9) Clark, G. R.; Gray, E. J.; Neidle, S.; Li, Y.-H.; Leupin, W. Isohelicity and Phasing in Drug−DNA Sequence Recognition: Crystal Structure of a Tris(benzimidazole)-Oligonucleotide Complex. *Biochemistry* **1996**, *35*, 13745−13752.

(10) Xu, Z.; Li, T.-K.; Kim, J. S.; LaVoie, E. J.; Breslauer, K. J.; Liu, L. F.; Pilch, D. S. DNA Minor Groove Binding-Directed Poisoning of Human DNA Topoisomerase I by Terbenzimidazoles. *Biochemistry* **1998**, *37*, 3558−3566.

(11) Pilch, D. S.; Liu, H.-Y.; Li, T.-K.; Kerrigan, J. E.; LaVoie, E. J.; Barbieri, C. M. Defining the Molecular Interactions that are Important for the Poisoning of Human Topoisomerase I by Benzimidazoles and Terbenzimidazoles. In *DNA and RNA Binders: From Small Molecules to Drugs*; Demeunynck, M., Bailly, C., Wilson, W. D., Eds.; Wiley-VCH: Weinheim, Germany, 2003; Vol. 2, pp 576−608.

(12) Jin, S.; Kim, J. S.; Sim, S.-P.; Liu, A.; Pilch, D. S.; Liu, L. F.; LaVoie, E. J. Heterocyclic Bibenzimidazole Derivatives as Topoisomerase I Inhibitors. *Bioorg. Med. Chem. Lett.* **2000**, *10*, 719−723.

(13) Sun, Q.; Gatto, B.; Yu, C.; Liu, A.; Liu, L. F.; LaVoie, E. J. Synthesis and Evaluation of Terbenzimidazoles as Topoisomerase I Inhibitors. *J. Med. Chem.* **1995**, *38*, 3638−3644.

(14) Griffith, J. *Methods in Cell Biology*; Academic Press: New York, 1973; p 129.

(15) Dimicoli, J.-L.; Hélène, C. Complex Formation Between Purine and Indole Derivatives in Aqueous Solutions: Proton Magnetic Resonance Studies. *J. Am. Chem. Soc.* **1973**, *95*, 1036−1044.

JM060520Q